Chemical Engineering Science 302 (2025) 120794

Contents lists available at ScienceDirect

Chemical Engineering Science

journal homepage: www.elsevier.com/locate/ces

Propagation rate and product modulation in SHS reactions via focused microwave heating

Keren Shi [a], Megan Bokhoor [b], Yujie Wang [a], Timothy P. Weihs [b], Michael R. Zachariah [a,*]

[a] *University of California, Riverside, CA 92521, USA*
[b] *Department of Materials Science and Engineering and Hopkins Extreme Materials Institute, Johns Hopkins University, Baltimore, MD 21218, USA*

ARTICLE INFO

Keywords:
Combustion synthesis
Microwave
Thermophysical properties
Combustion modulation

ABSTRACT

This study investigated how locally focused microwave (MW) energy can be used to manipulate the local burn rate and product composition in an SHS reaction. Ball milled Al/Zr/C composites were prepared by ink-printing and locally heated by a monopole MW antenna remotely. Color pyrometry and infrared thermometry were used to analyze the local burn rate and temperature profile of the combustion. The local induced heating by the microwave resulted in an acceleration of the local burn rate ($> 2.5\times$) from which an effective-activation energy of $\sim$ 30 kJ/mol was extracted. The burn rate under these various conditions were found to be independent of the measured heat flux to the pre-heating zone. This coupled wit the low value of the activation energy implies mass transfer control. Product analysis showed that the mole fraction of ZrC in the product increases with local burn rate. This study demonstrated localized MW energy offers the potential to dynamically modulate burn rate and modify spatial distribution of product formation in SHS reaction.

1. Introduction

Self-propagating high-temperature synthesis (SHS) has been extensively studied as a manufacturing method for carbides, borides and aluminides (Merzhanov, 1995; Kharatyan and Merzhanov, 2012; Evseev et al., 2022; Wisutmethangoon et al., 2009). SHS reactions between binary or ternary solid reactants of light elements (Al, C) and a transition metal (Ti, Zr), can generate a solid reaction wave also known as “glassless” combustion (Makino, 2001; Merzhanov, 1997). For the purpose of conceptualization, the combustion wave can be thought to comprise three zones, the pre-heating zone where no chemistry takes place and temperature varies from ambient to the ignition point. The reaction zone where elements mix and form compounds, and temperature rises from the ignition point to the adiabatic flame temperature. Finally, the cooling zone post-reaction where cooling of the product takes place (Makino, 2003). In this paper we consider how a focused MW source can be used to manipulate the reaction-front, from which we can extract properties of the SHS process or otherwise manipulate the products formed.

MW absorption occurs through various mechanisms but can be characterized as dielectric and magnetic loss processes quantified by the permittivity and permeability respectively, and the characteristic particle size. In a prior calculation study, we showed how metal and oxide coated core–shell spheres interact with MW (Biswas et al., 2020). For metal particles in the micron regime, typical of the length scales used in this study, it is the magnetic component of the MW field that does most of the heating through generation of eddy currents. However also shown in that study is that the native-oxide coating, particularly if it is semiconducting, can significantly enhance the MW absorption efficiency. This was demonstrated experimentally with the ignition of Ti nano particles, coated with a lossy TiO_2/TiN and contrasting that with Al coated with Al_2O_3. In the latter case despite the higher absorption cross-section of Al over Ti, only the Ti ignited. This result was attributed to the significantly higher absorption from the semiconducting TiO_2/TiN shell relative to the dielectric Al_2O_3 shell (Biswas et al., 2020; Kline et al., 2020).

In the context of an SHS process, prior work has shown that pre-heating of reactants can improve product composition and structure. Yeh et al. studied the conversion or formation rate of vanadium nitride (VN) synthesized by SHS reaction and found that preheating the sample to 200 °C can increase the conversion rate from 45 % to 90 % (Yeh et al., 2005). Zhu et al. studied NiAl formation under induction pre-heating and found that pre-heating results in reduction of product grain size and higher hardness (Zhu et al., 2011). The latter work suggests that MW

---

* Corresponding author.
E-mail address: mrz@engr.ucr.edu (M.R. Zachariah).

https://doi.org/10.1016/j.ces.2024.120794
Received 6 February 2024; Received in revised form 28 May 2024; Accepted 1 October 2024

might offer a similar effect. However, in our case we will restrict the heating to a local region by focusing, rather than the whole sample as will be demonstrated.

The SHS reaction for this study comprises three components: aluminum (Al), zirconium (Zr), and carbon (C) and was originally conceived in Al-rich chemistries to form an electrically conductive compound of zirconium carbide (ZrC) in a conductive Al matrix. Hu et al. studied the reaction mechanism of dried milled Al/Zr/C powders and found the product composition varied with Al content. The weight percentage of the resulting AlZr alloy and AlZrC alloy increases with Al content by inhibiting ZrC particle growth (Hu et al., 2012). Arlington et al. assembled the ball milled powder of the same elemental content with a polymer binder by additive manufacturing, and found the binder content and sample thickness can greatly change the burn rate and further alter the product composition (Arlington et al., 2021). By coupling in-situ synchrotron X-ray diffraction with nanocalorimetry, they determined that either high heating rate or quenching is necessary for complete reaction and formation of ZrC and Al (Arlington et al., 2022). To enhance both reactant reactivity and product electrical conductivity, Arlington et al. determined a stochiometric ratio of 2:1.2:1 for Al:Zr:C works best using physical vapor deposited thin foils [15]. Kline et al. studied the thermal properties of the additive manufactured samples with the same composition (Kline et al., 2021). In that study, temperature profiles obtained from color pyrometry were used as input to a Boddington equation (1) analysis to extract thermal properties (i.e. thermal diffusivity and activation energy) (Boddington et al., 1986).

$$\frac{d\eta}{dt} = \frac{\frac{T-T_0}{t_d-t_r} + \frac{dT}{dt} - \frac{\alpha}{v^2}\frac{d^2T}{dt^2}}{T_{ad} - T_0} \tag{1}$$

where η is the conversion rate. T_{ad} and T_0 are the adiabatic flame temperature of the SHS reaction and ambient temperature, respectively. t_r and t_d are rise and decay times for the reaction, α is the thermal diffusivity of the reactants and v is burn rate of the reaction. While this method has proved useful in calculating thermal properties, the accuracy of the results largely depends on the accessibility of the parameters in the Boddington equation (1) for the SHS reaction of interest (Boddington et al., 1986).

In this study, a new method that measures the effective activation energy from temperature sensitivity of the SHS reaction burn rate is demonstrated. Herein we show how using a local MW radiating antenna, a steady-state spatial temperature profile can be generated in a sample. When ignited the propagation velocity is seen to track the local temperature profile induced by the MW. Using imaging pyrometry in both the visible and infrared range we are able to obtain the complete reaction front temperature profile. Surprisingly, we observe that the measured heat flux from the reaction zone to the pre-heating zone is independent of the initial local temperature, implying heat conduction is not rate limiting. To determine whether the reaction rate or the diffusion rate controls the burn rate increase, a thermal Damköhler number is defined and suggests that the burn rate increase is related to the reaction rate increase rather than heat flux. An effective activation energy is calculated to be ~ 30 kJ/mol from the Arrhenius plot of local burn rate and initial surface temperature. The calculations confirm that this new approach can be used as an alternative way to estimate thermal properties and effective activity energies of composite samples. Product analysis shows that the composition of the desired product ZrC increases with burn rate. This study provides a novel method to extract thermophysical properties directly from temperature profiles of SHS reaction. The results show that this approach can be used as a tool to locally moderate burn rate and modifify spatially product composition in SHS reactions.

2. Experimental section

2.1. Materials

2Al:1.2Zr:C powder was created via a two-step milling procedure using a RETSCH PM 400 planetary mill. Al (Thermo Scientific, −325 mesh, 99.5 % purity), Zr (Atlantic Equipment Engineers, −20 + 60 mesh, 99 % purity), and 1/4-inch 420 stainless steel ball bearings (bearingballstore.com) were first combined in a 3:2 M ratio using hexane as the process control agent and a ball-to-powder ratio (BPR) of 3. The milling program consisted of 7.5 min of run time at 400 rpm followed by 15 min. of rest, repeated for a total of 450 min. The remaining Al, Zr, C (Sigma Aldrich, 2–12 μm, 99.95 % purity), hexane, and ball bearings were added to maintain at BPR of 3 and yield an overall stoichiometry of 2Al:1.2Zr:C. This was then milled using the same procedure as in step 1 and subsequently sieved to less than 32 μm. Cellulose acetate (average MW ~ 50,000) and N,N-Dimethylformamide (99.8 %) were purchased from Sigma Aldrich and Fisher Scientific, respectively. All materials were used as received.

2.2. Ink preparation and direct writing process

The ink preparation and printing process follows the procedures optimized by Kline et al. (Kline et al., 2021), although the polymer binder content was increased in this study. Direct writing ink was prepared by first dissolving 75 mg cellulose acetate in 1.4 mL N,N-Dimethylformamide and then adding 3600 mg of powder. The ink was then mixed for 2 min. at 2000 rpm to form a uniform slurry. The slurry was transferred to a 10 mL syringe with an 18-gauge Luer-Lock taper nozzle. Four layers were printed with Hyrel3D printer at an extrusion rate of 60 mm^3/min, to yield print lines of ~ 3 mm thickness (Fig. 1a). The printed sample were cut to 40 mm length sticks after drying. The polymer content was increased from 1.4 wt% to 2.0 wt% compared to our previous study to improve the ductility of the printed sample, and the samples were reacted on the glass substrates to minimize heat losses.

2.3. Microwave heating system

A microwave monopole antenna source was used to prepare a steady-state temperature profile in the Al/Zr/C samples prior to ignition (Shi et al., 2023). The microwave antenna (2 % thoriated tungsten electrode, length: 30 mm, ~1/4λ, diameter: 1 mm) was connected to a magnetron (MKS Instruments, MW head TM012) operating at 2.45 GHz (λ ~122 mm) by a WR340 cavity to coaxial transition adaptor. The Al/Zr/C samples were placed 8 mm below the microwave antenna on a glass substrate (Fig. 1b) with the MW source set to three power levels ~140 W, ~175 W and ~220 W. This enabled a steady-state peak pre-heat temperature in the samples of ~50 °C, ~100 °C and ~150 °C, respectively. The surface temperature was monitored in real time by an infrared camera (Telops, FAST M3K, exposure time: 20 μs, frame rate: 500 fps, spatial resolution: ~130 μm per pixel). After the peak temperature achieved steady-state for approximately 3 min, the sample was ignited at the right end with a secondary heat source, and the combustion was imaged with IR and color cameras simultaneously (Vision Research Phantom, Miro M110, exposure time: 350 μs, frame rate: 500 fps, spatial resolution: ~45 μm per pixel) from the 60° angled top-down view. The MW power remained on during combustion.

2.4. Local burn rate and reaction temperature measurements

The analyze the results, the color video images were binarized by a MATLAB routine to convert the reaction zone (pixel that detects light intensity from reaction) to white, and the unreacted zone (pixel without intensity) to black (Bradley and Roth, 2007). Then the position of the white color region was tracked at each frame. Local burn rates were calculated from the color video by the position of the reaction front-time

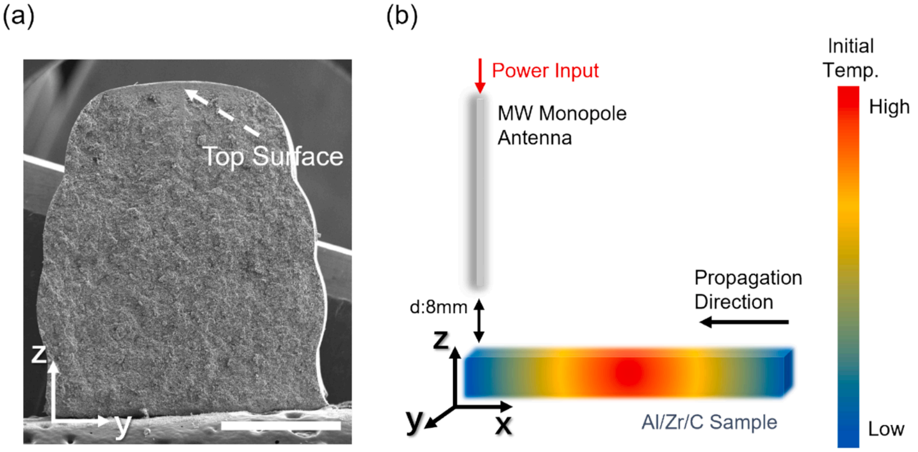

Fig. 1. (a) SEM image of YZ-plane of the printed Al/Zr/C sample. The analysis was focused on the top surface of the sample. (scale bar: 10 mm) (b) Experiment setup of the MW combustion test system. Color gradient represents the pre heated temperatures following remote MW heating. The sample was ignited at the right end and the combustion flame propagated from right to left.

relationship. Reaction temperature of the sample was obtained by color pyrometry and IR measurements. Color pyrometry uses the ratio of three channel intensities (red, green and blue) to extract temperature (Wang et al., 2024; Jacob et al., 2018), based on calibration from a blackbody source (Mikron M390). The color pyrometry allows temperature measurement > 1000 K, and IR imaging was used to extend the temperature measurement from 1000 to 800 K. The IR emissivity of the sample is estimated by fitting the spatial temperature from IR measurements to the color pyrometry temperature. The estimated emissivity at high temperatures is ~15 %. All experiments were repeated in triplicate unless otherwise stated.

2.5. *Sample characterization*

Scanning electron microscopy (SEM, ThermoFisher Scientific NNS450) with electron dispersive analysis (EDS, Oxford Instruments AztecSynergy) was used to characterize particle and elemental distribution of the ball milled powders and reaction products. ImageJ software (version 1.54d) was used to extract the equivalent spherical diameter of the irregular shaped powders from both reactant and product with sample a size of at least 150 particles. Product samples for X-ray diffraction (XRD, PANalytical Empyrean Series 2) using Cu Kα radiation source were divided into three regions based on surface temperature to investigate any product composition or crystal structure change with different initial temperature.

3. Results and discussion

3.1. *Local burn rate modulation with MW*

The burn rate of samples at room temperature (no MW) was first determined to obtain a baseline result. The burn rate was calculated by tracking the position of the flame front versus time as shown in Fig. S1. The local burn rate suggests that steady burning was achieved after ~2 s (~5 mm in length) then the sample burned at a constant velocity of ~1.6 mm/s in the absence of any MW heating. This linear burn rate behavior is consistent with previous results reported for 3D printed Al/Zr/C samples (Arlington et al., 2021; Kline et al., 2021). Previous results showed the propagation of the printed sample with 1.4 wt% polymer was 3.6 mm/s in argon environment (Kline et al., 2021). The decrease in burn rate in this study is attributed to a combination effect of polymer binder ratio increase and reaction environment change (Arlington et al., 2021; Wainwright et al., 2018). In the case with MW's, when the combustion wave propagated to the end of the sample, the high electric intensity from the source antenna and the smoke generated from the polymer binder causes discharge (Lebedev, 2010). Because of edge effects at the beginning of the sample and discharge at the end of the sample, burn rate data at the two terminals of the sample were not used for data analysis.

In our previous study, a receiving MW antenna was embedded in a poor MW sensitive Al/CuO nanocomposites to generate localized hot spots at the two terminals of the receiving antenna using the same monopole source antenna setup (Shi et al., 2023). Simulation confirmed that high electric fields induced at the two terminals of the receiving antenna are sufficient to generate hot spots in poor MW sensitive nanoparticles, and can lead to either ignition or modulation of the burn rate. However, in this study, with micron powders, heating by the magnetic component inducing eddy currents, thus enabling the 3D printed sample to be remotely heated with the monopole MW source antenna, and with sufficient power, to lead to ignition. Since the objective of this experiment was to explore the relationship of local burn rate and local pre-heating temperature, the MW power was carefully tuned to only generate a hot spot along the sample, without any pre-ignition reactions. As such, peak pre-heating temperatures of ~50 °C, ~100 °C and ~150 °C were chosen because they are lower than temperatures where exothermic reactions of the polymer binder (Fig. S2) or ball-milled powder (Hu et al., 2012) were observed during thermogravimetric analysis. Fig. 2(a) shows the spatial distribution of steady-state temperature that can be achieved with the MW source tuned to achieve a nominal peak temperature of ~50 °C. In the same figure, we overlay the spatial distribution of burn rate. Clearly the measured local burn rate tracks the general features of the temperature profile induced by the MW source. The local burn rate peaks at ~ 2.7 mm/s at the position of peak initial surface temperature, and is 70 % faster than the baseline burn rate. When the initial peak temperature is increased to ~100 °C and ~150 °C, the peak local burn rate increases to ~3.3 mm/s and ~4.2 mm/s, respectively, and one sees a similar local burn rate correlation with the initial surface temperature profile. (Fig. 2(b) and (c)). This is a clear demonstration of the use of focused microwave radiation to modulate and tune burn rate.

3.2. *Reaction front temperature profiles*

Color pyrometry and IR thermometry were used to analyze the temperature profile during the SHS reaction. Fig. 3 shows the reaction front temperature profiles during combustion for the four cases studied. (Fig. S3 plots the temperature profile as divided into pre-heating zone, reaction zone and cooling zone based on temperature). One important point is that while we can see significant enhancement in the propagation velocity of ~ 2.5 ×, the measured peak temperatures do not show a

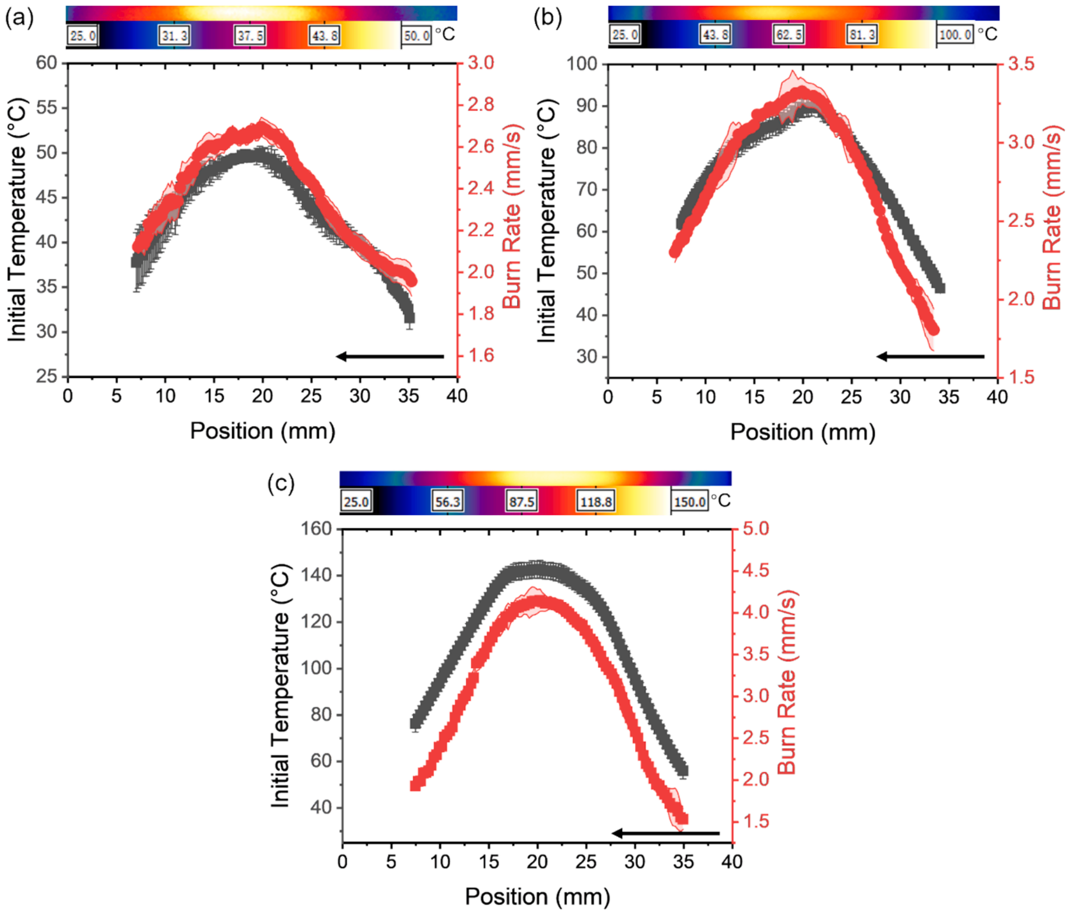

Fig. 2. IR images (top) of steady-state initial MW induced temperature profiles and spatial distribution of initial local temperatures and burn rates for peak initial temperatures of (a) ~50 °C, (b) ~100°C and (c) ~150 °C. Flame propagation is from right to left as indicated by the arrow.

significant change. The peak temperatures are all roughly in the ~ 1700 K region, and any observable changes are within the uncertainty in our experimental measurement (±110 K), such that trends have not been inferred. Also, the observed peak flame temperature agrees with the calculated adiabatic flame temperature of the 2Al:1.2Zr:1C formation reaction of 1770 K[21]. The lengths of the pre-heating zone (obtained from exponential fitting of temperature profile from 800 K to 933 K) are 510 ± 75 μm and do not change significantly with initial temperature. The lengths of the leading edge of the reaction zone from 933 K to the maximum flame temperature range from 1.0 mm to 1.5 mm in all cases. However, the trailing edge of the flame (from the maximum flame temperature to 933 K) clearly increases in length with increasing MW power. The length of the trailing edge is 7–8 mm without MW heating, but is clearly wider under MW stimulation. Since the product of the reaction shows low MW sensitivity, the increase in length of the trailing edge we attribute to reaction intermediates (typically ZrAlC alloy) absorbing MW energy during flame propagation.

3.3. Damköhler number, thermal diffusivity, and effectivity activation energy

Here we consider extraction of kinetic parameters. According to premixed flame theory, the burn rate can be expressed by equation (2) (Mallard; Le Chatelier, 1885; Law, 2010):

$$v \propto \sqrt{\alpha^* \omega} \tag{2}$$

where v is the local burn rate, α is thermal diffusivity and ω is reaction rate.

The general character of this theory has been applied to SHS systems (Kanury and Hernandez-Guerrero, 1994; Mukasyan and Shuck, 2017). Since there are two variables in equation (2) we can explore deconvolving this dependence to gain some mechanistic insight.

We begin by defining a thermal Damköhler number (Da) as in equation (3):

$$Da = \frac{q_{rxn}}{q_{diff}} \frac{ReactionRate}{DiffusionRate} \tag{3}$$

where $q_{rxn} = v^* \Delta H_{rxn}{}^* \rho$ represents the heat flux generated by the reaction; v is local burn rate, ΔH_{rxn} is −1905 J/g for ZrC formation (Song et al., 2009) based on fact that ZrC is the main product formed; and ρ is the density of the printed sample. $q_{diff} = \alpha^* \rho^* C_p{}^* \frac{dT}{dx}_{PHZ}$ characterizes the heat flux from the reaction zone to the pre-heating zone (PHZ), where $dT/dxPHZ$ is the temperature gradient at 933 K determined from the measured temperature profile under reaction conditions, (dashed line in Fig. S3) since the reaction is initiated by Al melting (Hu et al., 2012). α is the thermal diffusivity, C_p is the specific heat capacity at the initial surface temperature. The thermal diffusivity in this system can be determined by evaluating the components in the heat diffusion equation (4):

$$\frac{dT}{dx} = \frac{\alpha}{v}\left(\frac{d^2T}{dx^2}\right) \tag{4}$$

Where v is the local burn rate. dT/dx and d^2T/dx^2 are the first and second derivatives obtained by fitting the experimentally measured temperature profiles in the pre-heating zone (PHZ), shown in Fig. 3. Table 1 lists the resulting thermal diffusivity calculated from temperature profiles for the four initial temperature conditions.

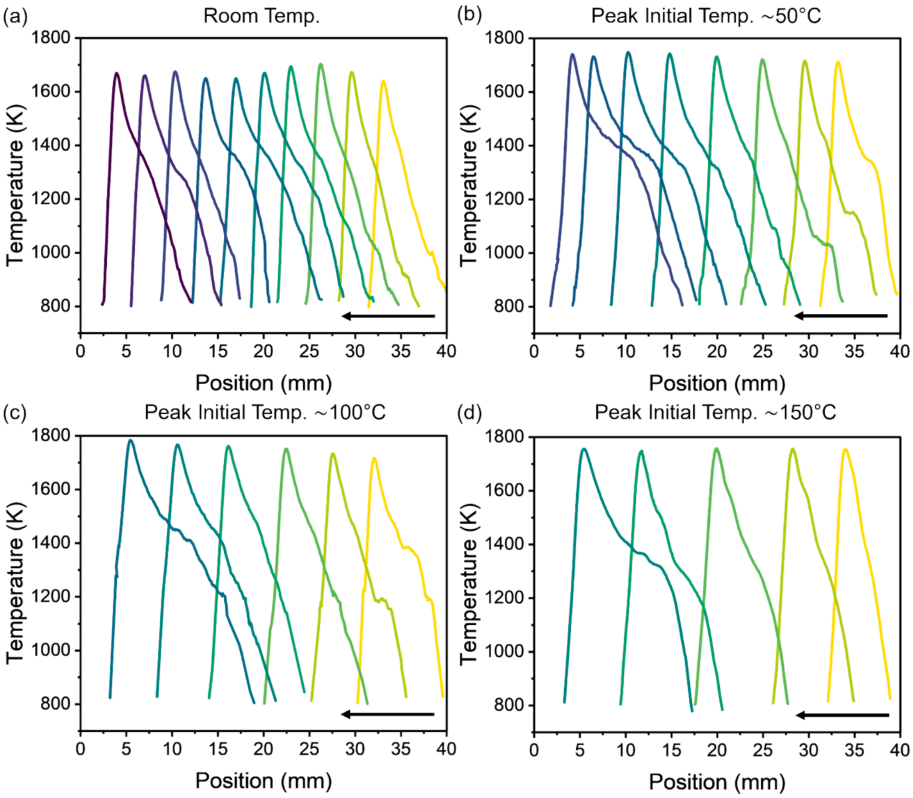

Fig. 3. Temperature profiles of combustion waves for different initial peak temperatures: (a) room temperature (without MW heating), (b) ~50 °C, (c) ~100 °C and (d) ~150 °C. The time gap between each profile is 2 s. Propagation direction was from right to left and indicated by the arrow.

Table 1
Thermal diffusivity from temperature profile at different initial surface temperatures.

Initial surface temperature (°C)	R.T.	~50 °C	~100 °C	~150 °C
Ave. thermal diffusivity ($\times 10^{-6}$ m^2/s)	2.1 ± 0.4	1.8 ± 0.4	2.0 ± 0.2	2.3 ± 0.2

The calculated thermal diffusivities are approximately the same for the four conditions systems at ~ 2.0×10^{-6} m^2/s, and comparable to our previous estimates of 2.2×10^{-6} m^2/s obtained from the Boddington equation (1) through the temperature profile (Kline et al., 2021).

Fig. 4 plots dT/dx_{PHZ} versus local burn rate at an initial peak temperature of ~50 °C, ~100 °C and ~150 °C. Most of the data points evaluated (from Fig. 3) for the flame to pre-heating zone yield thermal gradients of 600 – 800 K/mm, and with no discernable trend, i.e. *independent of burn rate*. This is a surprising result as it implies that the burn velocity is not dependent on the heat conduction from the burned region to the unburned region, which in a sense contrary to the basic premise of laminar flame theory as presented in equation (2). More insights can be gained by evaluating the Damköhler number.

With all the parameters obtained, the Damköhler number can now be calculated and is plotted versus the local burn rate in Fig. 5. In all cases the Damköhler number is > 1, and increasing with local burn rate. This indicates that the reaction term dominates heat flux as the local burn rate increases. This is consistent with the fact that the heat flux does not depend on burn rate as described above from the results in Fig. 4.

From equation (2), we can further assume the reaction rate follows Arrhenius behavior as expressed in equation (5):

$$v \propto \sqrt{\alpha^* A^*} e^{-\frac{Ea_{eff}}{2RT}} \tag{5}$$

An effective activation energy can be calculated from the Arrhenius plot of local burn rate and initial surface temperature. Fig. 6 shows that the data are clearly Arrhenius in nature, with an average effective activation energy of 29.4 kJ/mol. This energy is much lower than the reported chemical activation energy (99–186 kJ/mol) using thermal analysis (Kline et al., 2021; Mukasyan and Shuck, 2017). However, the reader is reminded that this an effective activation energy, and is similar to that calculated using the Boddington equation (1) (31 ± 4 kJ/mol) and reflects the sensitivity of burn rate to the initial temperature of the printed sample (Kline et al., 2021; Drennan and Brown, 2024). Since heat flux does not appear to be a limiting parameter based on Damköhler number, and the activation energy is much too low for chemical reaction control, we are left to conclude that the process must be mass transfer controlled. (i.e. intermixing of reactants)

This effective activation energy may represent the diffusion of Zr in liquid Al. Although lacking experimental data for the diffusion activation energy of Zr in liquid Al, diffusion activation energies of period IV transition metals in liquid Al are reported to range from 18 – 36 kJ/mol (Du et al., 2003). The rate limiting step at 30 wt% Al content in Al/Zr/C composites (Hu et al., 2012) is thought to be the alloying reaction between Al and Zr. Mass transfer limited by particle to particle contact and retardation by the polymer matrix may also play a role.

Using the Boddington equation (1) to extract thermal properties of SHS reaction would have necessitated using the adiabatic flame temperature, and the rise and decay time of the reaction as shown in equation (1). By contrast, the approach presented here provides a facile and alternative method to extract thermal properties from a temperature profile and enables estimation of temperature sensitivity of composites system.

3.4. Post combustion product analysis

Since the local burn rates track the surface temperature distributions, the reacted samples were divided into three regions (by temperature)

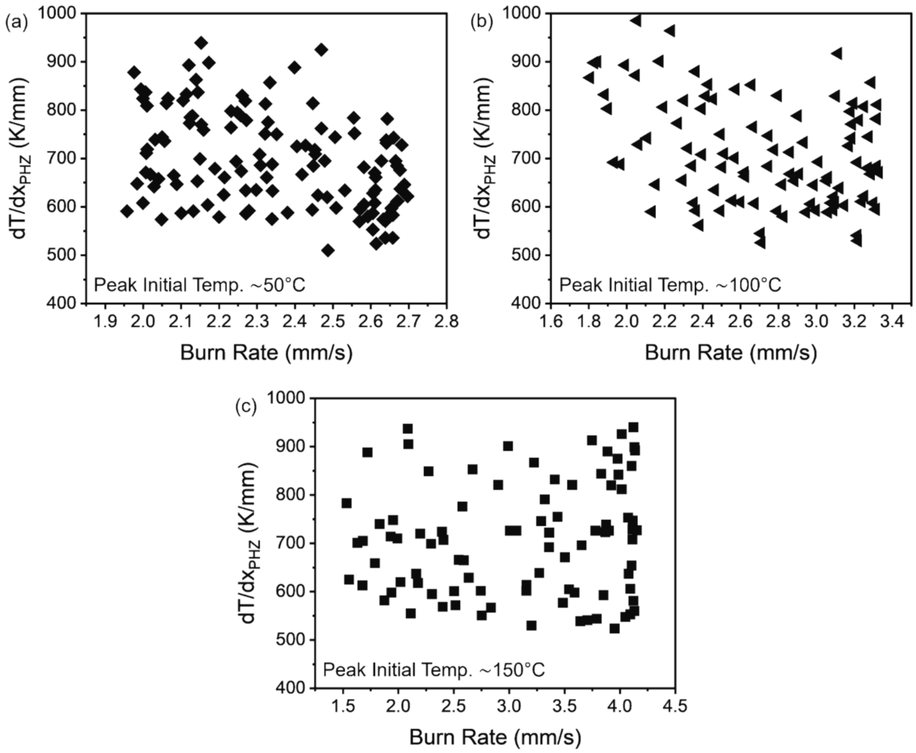

Fig. 4. Temperature gradient (proportional to heat flux) evaluated from Fig. 3 profiles from reaction zone to pre-heating zone (PHZ) at 933 K. For initial peak surface temperature of (a) ~50 °C, (b) ~100 °C and (c) ~150 °C.

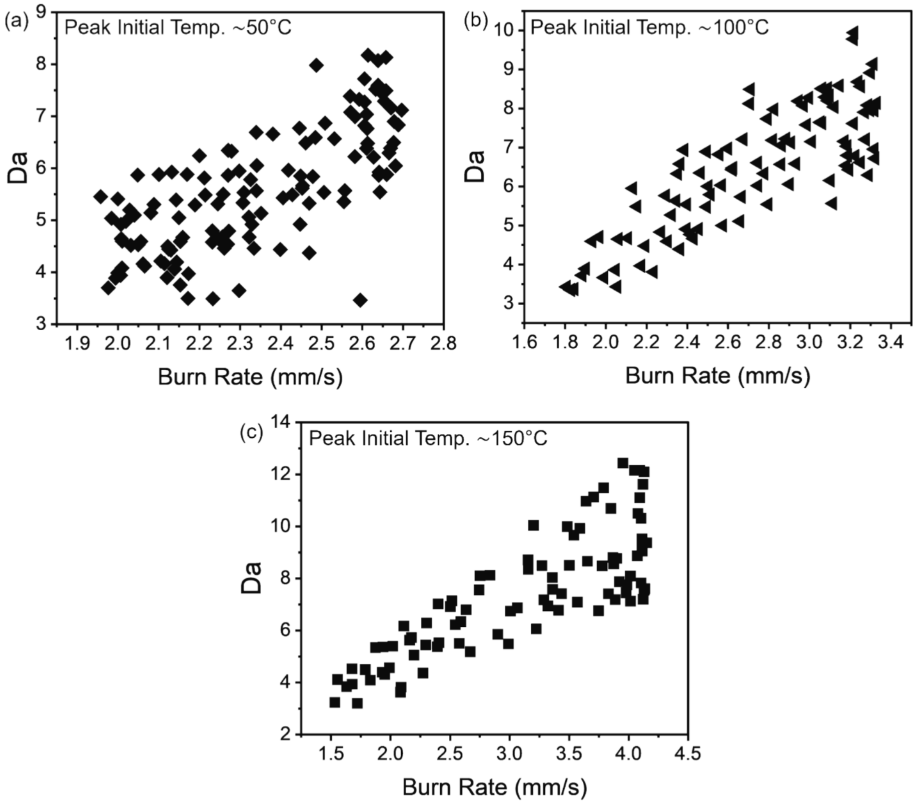

Fig. 5. Damköhler number of initial peak surface temperature of (a) ~50 °C, (b) ~100 °C and (c) ~150 °C. All Damköhler numbers increase with local burn rates, indicating that the local burn rate increases are controlled by the reaction rate.

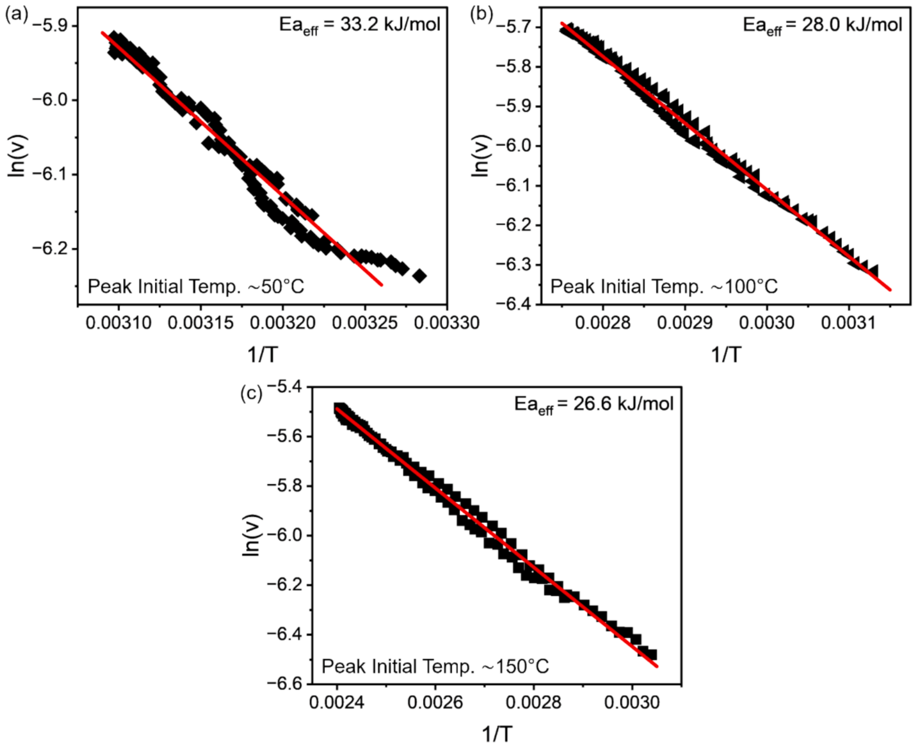

Fig. 6. Effective activation energy for burn rate (a) ~50 °C, (b) ~100 °C and (c) ~150 °C. The average effective activation energy is 29.4 kJ/mol.

and analyzed by SEM-EDS and XRD. The XRD of the as-milled powder shows separate Al, Zr and C phases and indicates no reaction occurred in the milling process (Fig. S4). The XRD of post combustion products reacted without MW heating shows the presence of Al, ZrO_2, Al_3Zr and ZrC (Fig. 7(a)). Since the combustion was done in an ambient environment, oxygen also reacted with Zr and formed ZrO_2 in the sample combusted without MW heating. Alumina is also likely to form during the same process, however no crystalline phase of alumina was detected. With MW heating to ~50 °C, ~100 °C and ~150 °C. It is clear that the crystalline zirconia phase was not detected, and the formation of alumina may also be inhibited. The intensity of the ZrC phase increased with initial temperature. With increasing initial temperature, the intensity of the ZrC peak at ~39° relative to the Al_3Zr peak at ~38° increases. Rietveld refinement done on the XRD pattern from 10° to 80°, and the results of the center region at different initial peak temperatures are plotted in Fig. 7(b) (Doebelin and Kleeberg, 2015). The results show that the main product is ZrC with MW heating. SEM images in Fig. 8 and size distribution in Fig. S5 show the powders shape and size have no significant change before and after reaction, and the EDS maps in Figs. S6–S10 show that Al and Zr are evenly distributed in the same particle, confirming the XRD results. However, the weight percentage of ZrC and Al in the center (heated) region increases with increasing initial peak temperature. And the weight percentage of ZrC and Al also vary in the different regions in the same sample (Fig. S11), with ZrC and Al at the highest percentage in the center region, which corresponds to the location of highest local burn rate. This increase in the ZrC formation correlates with increasing local burn rate, which confirms the Damköhler number calculation that reaction rate gradually increase with local burn rate therefore leads to more complete reaction. These results suggest that localized MW heating can be used to alter the final product and physical properties (i.e. hardness and resistivity) in a single Al/Zr/C sample by increasing the formation of ZrC and inhibiting the formation of metal oxides. MW heating also offers the potential to be applied to other SHS reactions since most of the SHS reactions contain metal elements which are MW sensitive in micro size region.

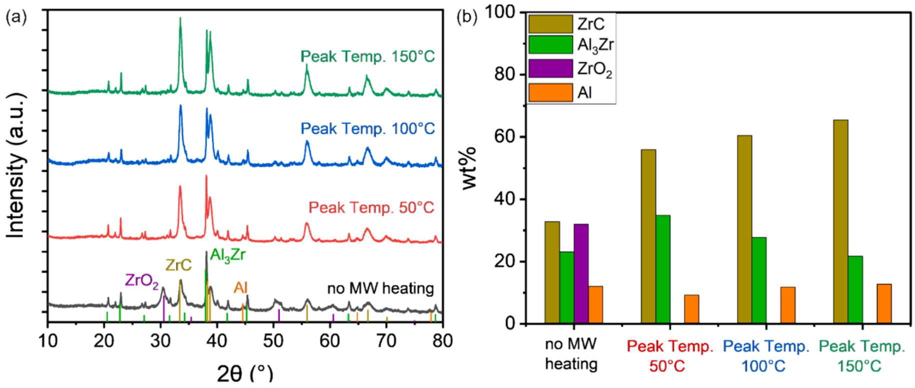

Fig. 7. (a) XRD pattern of the product from the center region of the sample reacted with different pre-heating temperatures. The intensity is normalized with the Al_3Zr peak at 2θ ~ 38.1°. (b) Weight fractions of different phases determined by Rietveld refinement.

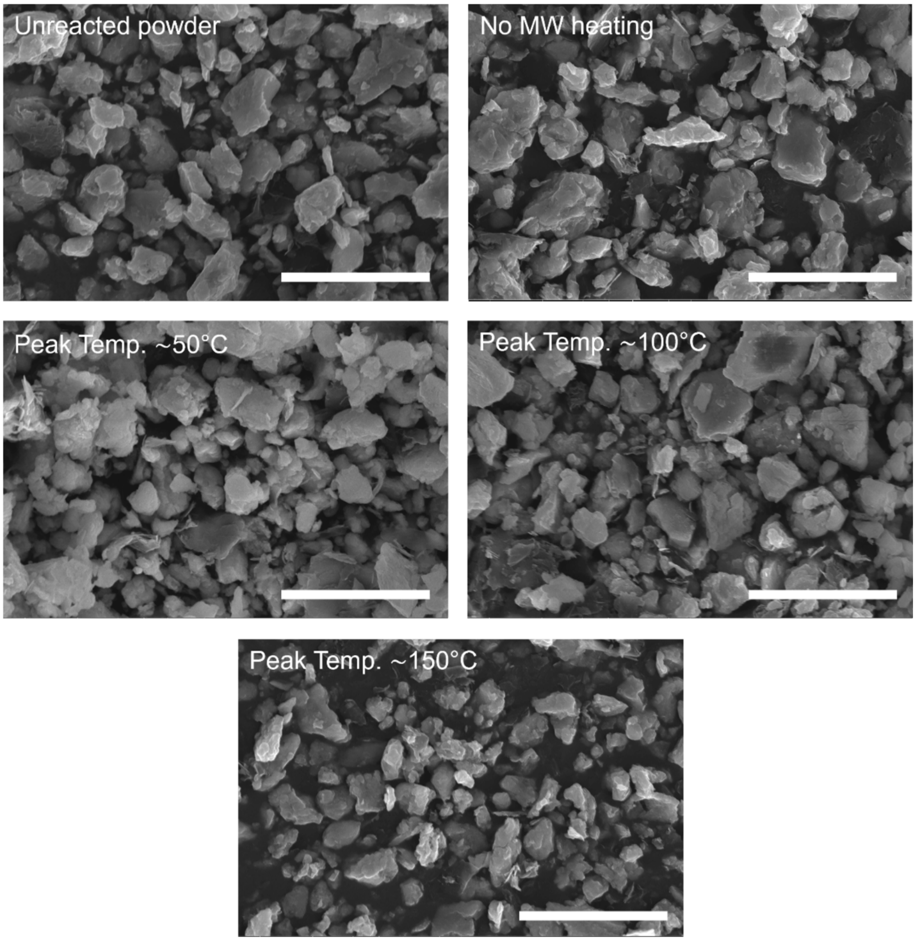

Fig. 8. SEM images of unreacted powders and products after reaction at different initial surface temperatures. (Scale bar: 10 μm).

4. Conclusions

This study investigates how the propagation rate, thermal properties, and product phases of 3D-printed Al/Zr/C composites can be manipulated with microwave heating, and how transport and reactive properties can be extracted from a single experiment. Microwave energy directed from an antenna is able to generate a steady state temperature profile which correlated to the local burn rate. The local burn rate was increased up to 2.5x with a ~150 °C pre-heating temperature. Color pyrometry and IR thermometry were used to measure the temperature profile within the pre-heating and reaction zones, and the thermal diffusivity in the pre-heating zone was determined to be $\sim 2 \times 10^{-6}$ m^2/s. The measured temperature gradient in the preheating zones was found to be in the range of 600——800 K/mm, and independent of burn rate, implying that propagation was not thermal transport limited. An effective activation energy representing the temperature sensitivity of the burn rate is ~ 30 kJ/mol. Post products analysis showed that ZrC content increases with local burn rate by localized MW energy and the products formation can be altered in a single sample. This study provides a new approach to estimate the thermal properties of SHS materials, and to measure the temperature sensitivity of reaction by effective activation energy. Product composition in the same sample can be altered via hot spots generated by MW energy. This localized MW heating approach also has the potential to apply to SHS reaction involving metal elements.

CRediT authorship contribution statement

Keren Shi: Writing – original draft, Data curation. **Megan Bokhoor:** Data curation. **Yujie Wang:** Data curation. **Timothy P. Weihs:** Writing – review & editing. **Michael R. Zachariah:** Writing – review & editing, Supervision, Resources, Project administration, Methodology, Investigation, Funding acquisition, Conceptualization.

Declaration of competing interest

The authors declare that they have no known competing financial interests or personal relationships that could have appeared to influence the work reported in this paper.

Data availability

Data will be made available on request.

Acknowledgements

The authors thank the support from an AFOSR - MURI and a DTRA-Materials Science in Extreme Environments URA.

Appendix A. Supplementary data

Supplementary data to this article can be found online at https://doi.org/10.1016/j.ces.2024.120794.

References

Arlington, S.Q., Barron, S.C., DeLisio, J.B., Rodriguez, J.C., Vummidi Lakshman, S., Weihs, T.P., Fritz, G.M., 2021. Multifunctional reactive nanocomposites via direct ink writing. Adv Materials Technologies 6 (5), 2001115. https://doi.org/10.1002/admt.202001115.

Arlington, S.Q., Neuhauser, T., Short, M., Woll, K., LaVan, D.A., Fritz, G.M., Weihs, T.P., 2022. Leveraging high heating rates to attain desirable reaction products in Al/Zr/C nanocomposites. Materials & Design, 111514. https://doi.org/10.1016/j.matdes.2022.111514.

Biswas, P., Mulholland, G.W., Rehwoldt, M.C., Kline, D.J., Zachariah, M.R., 2020. Microwave absorption by small dielectric and semi-conductor coated metal particles. Journal of Quantitative Spectroscopy and Radiative Transfer 247, 106938. https://doi.org/10.1016/j.jqsrt.2020.106938.

Boddington, T., Laye, P.G., Tipping, J., Whalley, D., 1986. Kinetic analysis of temperature profiles of pyrotechnic systems. Combustion and Flame 63 (3), 359–368. https://doi.org/10.1016/0010-2180(86)90005-2.

Bradley, D., Roth, G., 2007. Adaptive thresholding using the integral image. Journal of Graphics Tools 12 (2), 13–21. https://doi.org/10.1080/2151237X.2007.10129236.

Doebelin, N., Kleeberg, R., 2015. Profex : A Graphical User Interface for the Rietveld Refinement Program BGMN. J Appl Crystallogr 48 (5), 1573–1580. https://doi.org/10.1107/S1600576715014685.

Drennan, R. L.; Brown, M. E. Binary and Ternary Pyrotechnic Systems of Mn and/or MO and Ba02 and/or Sr02. Part 3. Kinetic Aspects.

Du, Y., Chang, Y.A., Huang, B., Gong, W., Jin, Z., Xu, H., Yuan, Z., Liu, Y., He, Y., Xie, F.-Y., 2003. Diffusion coefficients of some solutes in Fcc and liquid Al: critical evaluation and correlation. Materials Science and Engineering: A 363 (1–2), 140–151. https://doi.org/10.1016/S0921-5093(03)00624-5.

Evseev, N.S., Matveev, A.E., Nikitin, P.Y., Abzaev, Y.A., Zhukov, I.A., 2022. A theoretical and experimental investigation on the SHS synthesis of (HfTiCN)-TiB2 high-entropy composite. Ceramics International 48 (11), 16010–16014. https://doi.org/10.1016/j.ceramint.2022.02.144.

Hu, Q., Zhang, M., Luo, P., Song, M., Li, J., 2012. Thermal explosion synthesis of ZrC particles and their mechanism of formation from Al–Zr–C elemental powders. International Journal of Refractory Metals and Hard Materials 35, 251–256. https://doi.org/10.1016/j.ijrmhm.2012.06.008.

Jacob, R.J., Kline, D.J., Zachariah, M.R., 2018. High speed 2-dimensional temperature measurements of nanothermite composites: probing thermal vs. gas generation effects. Journal of Applied Physics 123 (11), 115902. https://doi.org/10.1063/1.5021890.

Kanury, A.M., Hernandez-Guerrero, A., 1994. Steady planar propagation of the gasless SHS reaction producing titanium carbide. Combustion Science and Technology 102 (1–6), 1–19. https://doi.org/10.1080/00102209408935467.

Kharatyan, S.L., Merzhanov, A.G., 2012. Coupled SHS reactions as a useful tool for synthesis of materials: an overview. Int. J Self-Propag. High-Temp. Synth. 21 (1), 59–73. https://doi.org/10.3103/S1061386212010074.

Kline, D.J., Rehwoldt, M.C., Turner, C.J., Biswas, P., Mulholland, G.W., McDonnell, S.M., Zachariah, M.R., 2020. Spatially focused microwave ignition of metallized energetic materials. Journal of Applied Physics 127 (5), 055901. https://doi.org/10.1063/1.5134089.

Kline, D.J., Rehwoldt, M.C., DeLisio, J.B., Barron, S.C., Wang, H., Alibay, Z., Rodriguez, J.C., Fritz, G.M., Zachariah, M.R., 2021. In-operando thermophysical properties and kinetics measurements of Al-Zr-C composites. Combustion and Flame 228, 250–258. https://doi.org/10.1016/j.combustflame.2020.12.045.

Law, C.K., 2010. Combustion physics. Cambridge University Press.

Lebedev, Y.A., 2010. Microwave discharges: generation and diagnostics. J. Phys.: Conf. Ser. 257, 012016. https://doi.org/10.1088/1742-6596/257/1/012016.

Makino, A., 2001. Fundamental aspects of the heterogeneous flame in the self-propagating high-temperature synthesis (SHS) process. Progress in Energy and Combustion Science 27 (1), 1–74. https://doi.org/10.1016/S0360-1285(00)00004-6.

Makino, A., 2003. Heterogeneous flame propagation in the self-propagating, high-temperature, synthesis (SHS) process in multi-layer foils: theory and experimental comparisons. Combustion and Flame 134 (3), 273–288. https://doi.org/10.1016/S0010-2180(03)00090-7.

Mallard; Le Chatelier, 1885. Recherches sur la combustion des mélanges gazeux explosifs. J. Phys. Theor. Appl. 4 (1), 59–84. https://doi.org/10.1051/jphystap:01885004005901.

Merzhanov, A.G., 1995. History and recent developments in SHS. Ceramics International 21 (5), 371–379. https://doi.org/10.1016/0272-8842(95)96211-7.

Merzhanov, A.G., 1997. Fundamentals, achievements, and perspectives for development of solid-flame combustion. Russ Chem Bull 46 (1), 1–27. https://doi.org/10.1007/BF02495340.

Mukasyan, A.S., Shuck, C.E., 2017. Kinetics of SHS reactions: a review. Int. J Self-Propag. High-Temp. Synth. 26 (3), 145–165. https://doi.org/10.3103/S1061386217030049.

Shi, K., Wang, Y., Xu, F., Zachariah, M.R., 2023. Remote microwave heating and ignition with an embedded receiving antenna within nanocomposites. Chemical Engineering Science 280, 118948. https://doi.org/10.1016/j.ces.2023.118948.

Song, M.S., Huang, B., Zhang, M.X., Li, J.G., 2009. In situ synthesis of ZrC particles and its formation mechanism by self-propagating reaction from Al–Zr–C elemental powders. Powder Technology 191 (1–2), 34–38. https://doi.org/10.1016/j.powtec.2008.09.005.

Wainwright, E.R., Schmauss, T.A., Vummidi Lakshman, S., Overdeep, K.R., Weihs, T.P., 2018. Observations during Al: Zr composite particle combustion in varied gas environments. Combustion and Flame 196, 487–499. https://doi.org/10.1016/j.combustflame.2018.06.026.

Wang, H.; Julien, B.; Kline, D. J.; Alibay, Z.; Rehwoldt, M. C.; Rossi, C.; Zachariah, M. R. Probing the Reaction Front of Nanolaminates at ~µs Time and ~µm Spatial Resolution.

Wisutmethangoon, S., Denmud, N., Sikong, L., 2009. Characteristics and compressive properties of porous NiTi alloy synthesized by SHS technique. Materials Science and Engineering: A 515 (1–2), 93–97. https://doi.org/10.1016/j.msea.2009.02.055.

Yeh, C.L., Chuang, H.C., Liu, E.W., Chang, Y.C., 2005. Effects of dilution and preheating on SHS of vanadium nitride. Ceramics International 31 (1), 95–104. https://doi.org/10.1016/j.ceramint.2004.03.043.

Zhu, X., Zhang, T., Marchant, D., Morris, V., 2011. The structure and properties of NiAl formed by SHS using induction heating. Materials Science and Engineering: A 528 (3), 1251–1260. https://doi.org/10.1016/j.msea.2010.10.002.